

A HYDRODYNAMIC EVALUATION OF THE
SANDIA UO₂ EQUATION OF STATE EXPERIMENT

by

Mark Scott Smith

A Thesis Submitted to the Faculty of the
DEPARTMENT OF NUCLEAR ENGINEERING
In Partial Fulfillment of the Requirements
For the Degree of
MASTER OF SCIENCE

In The Graduate College
The University of Arizona

STATEMENT BY AUTHOR

This thesis has been submitted in partial fulfillment of requirements for an advanced degree at The University of Arizona and is deposited in the University Library to be made available to borrowers under rules of the Library.

Brief Quotations from this thesis are allowable without special permission, provided that accurate acknowledgment of source is made. Requests for permission for extended quotation from or reproduction of this manuscript in whole or in part may be granted by the head of the major department or the Dean of the Graduate College when in his judgment the proposed use of the material is in the interests of scholarship. In all other instances, however, permission must be obtained from the author.

SIGNED: Mark Scott Smith

APPROVAL BY THESIS DIRECTOR

This thesis has been approved on the date shown below:

Barry Ganapol
Barry Ganapol

Associate Professor of
Nuclear and Energy Engineering

Oct 29, 1981
Date

TABLE OF CONTENTS

	Page
LIST OF ILLUSTRATIONS	iv
LIST OF TABLES	vi
1. INTRODUCTION	1
2. ELECTRON BEAM EXPERIMENT	3
Experimental Procedure	3
Determination of UO ₂ Vapor Pressure	5
Experimental Results	8
3. THE FARA CODE	13
Numerical Methods	14
Benchmarking	18
4. NUMERICAL ANALYSIS	30
Results	30
Discussion	30
5. CONCLUSION	41
APPENDIX A: INPUT DESCRIPTION	43
REFERENCES	48

LIST OF ILLUSTRATIONS

Figure	Page
1. Schematic View of the Pulsed Vaporization Experiment	4
2. Schematic Diagram of the Streak Recording System and an Example of the Experimental Record	6
3. Electron Energy Absorption Profile as a Function of Mass Depth	7
4. Velocity as a Function of Time for Five Energy Pulses	9
5. Vapor Pressure as a Function of Internal Energy	10
6. Ackerman's and Menzies' EOS Plots Using Two Heat Capacity Models	12
7. Energy Input Benchmark	20
8. Frictional Flow Benchmark	22
9. Heat Transfer Benchmark	24
10. Shock Tube Benchmark	26
11. Rarefaction Benchmark	28
12. Comparison of Experimental Fit to Numerical Results for the 1860 J/g Energy Pulse	31
13. Comparison of Experimental Fit to Numerical Results for the 1990 J/g Energy Pulse	32
14. Comparison of Experimental Fit to Numerical Results for the 2030 J/g Energy Pulse	33
15. Velocity as a Function of Time for Two Au Sample Configurations	36
16. Comparison of Numerical Results Using Benson's and Menzies' EOS Models for 1860 J/g Energy Pulse	38
17. Comparison of Numerical Results Using Benson's EOS and Menzies EOS with Three Heat Capacity Models for 1990 J/g Energy Pulse	39

LIST OF ILLUSTRATIONS--Continued

Figure	Page
18. Comparison of Numerical Results Using Benson's EOS and Menzies EOS with Three Heat Capacity Models for 2030 J/g Energy Pulse	40

LIST OF TABLES

Table	Page
1 Vapor Pressure as a Function of Specific Energy	11

CHAPTER 1

INTRODUCTION

The safety of nuclear systems is a question of paramount importance to the people of the world. In particular fast reactor safety, because of the enormous energy potential of the system, is critical. A facet of fast reactor safety analysis centers on the postulated hypothetical core disruptive accident (HCDA). Accident termination may be achieved by core disassembly due to vapor pressure driven core expansion. Based on a postulated core disassembly and resulting core expansion, estimates can be made for radioactive release due to a breach in the LMFBR containment. In general, core disassembly analysis is composed of three models: 1) core hydrodynamic motion, 2) neutronics, and 3) core thermodynamic behavior. This work relates to the modeling of core thermodynamics during a postulated core disruptive accident.

An equation of state (EOS) is the focal point of thermodynamic modeling; it provides the pressure-temperature-volume relationship of the core materials. At Sandia Laboratories, volume heating experiments have been performed to obtain a data base for the EOS for fuel. Vapor pressure data has been obtained up to 5000K using electron beam (e-beam) heating of powered UO_2 samples. Previous UO_2 information has been based upon relatively low temperature measurements, using techniques like

vapor diffusion, transpiration and spectroscopic methods; however, there is little data in the 3000K to 6000K temperature range.

A comparison of e-beam results to other extrapolated and measured EOS models shows significant discrepancies. Therefore, the main objective of this thesis is to model the electron beam heating experiment from a hydrodynamic point of view in order to attempt to understand these discrepancies. To achieve this goal, the code FARA will be employed. FARA was designed to test the addition of fuel-structure heat transfer to the Eulerian disassembly code VENUS-III. FARA is an Eulerian, one dimensional, multicomponent fluid flow code with modifications for energy input and boundary motion.

A description of the electron beam experiment and a presentation of results follows in chapter two. Chapter three will detail the workings of the FARA code, including a discussion of the solution algorithm and several benchmark problems. A comparison of numerical and experimental results will be presented in the fourth chapter. The author's conclusion will be stated in the final chapter.

CHAPTER 2

ELECTRON BEAM EXPERIMENT

The following chapter is a discussion of the experimental procedure, of how UO_2 vapor pressure was determined, and of experimental results.

2.1 Experimental Procedure

The UO_2 experiment (Benson 1977) is designed to use the Sandia Relativistic Electron Beam Accelerator (REBA). By employing this accelerator, electron energy in excess of 20 kJ can be delivered to the target plane in a short time. By varying the beam cross sectional area, a specific energy absorbed by the target may be selected over a range of low levels to greater than 4000 J/gm. The energy pulse is approximately Gaussian in time with a 0.6 microsecond Full Width at Half Maximum (FWHM) duration.

The experimental apparatus is shown in Figure 1. A powdered UO_2 sample is confined between two graphite pistons which are pressed into a graphite cylinder. Piston mass density (mass/area) is 0.092 gm/cm² and the smeared sample density is 2.0 gm/cm³ with an estimated error of 50-80 percent. The sample was hyperstoichiometric with an oxygen to metal ratio of 2.08. Sample thickness varied from 30 microns to 225 microns. The graphite crucible was positioned in the electron

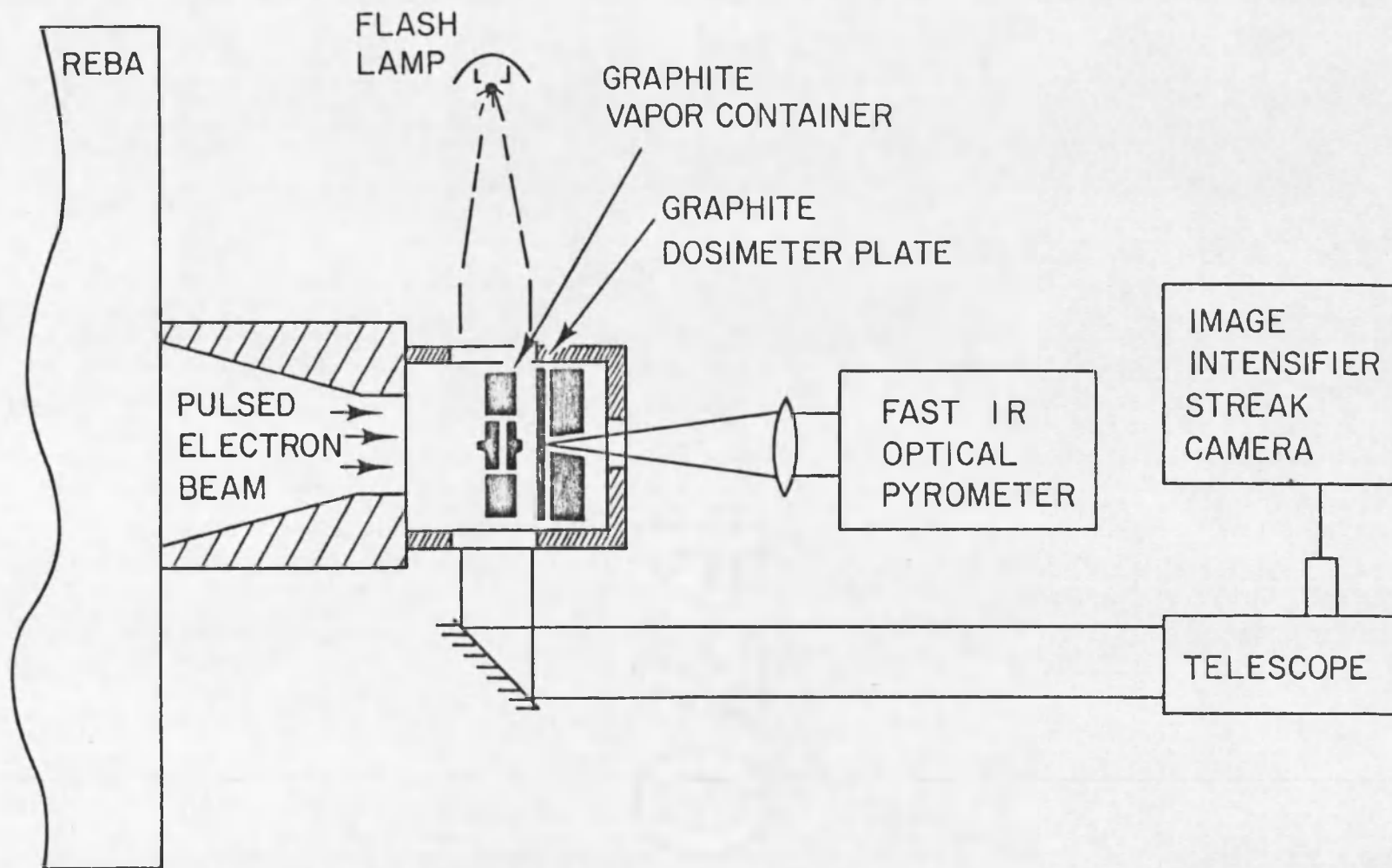


Fig. 1. Schematic View of the Pulsed Vaporization Experiment

beam path where it was heated by an electron pulse. Piston motion was a result of vapor pressure corresponding to the specific energy absorbed by the sample.

2.2 Determination of UO_2 Vapor Pressure

Two quantities were measured during this experiment, vapor pressure and sample specific energy. Vapor pressure was determined by means of streak photography of the normal displacement of the pistons (Figure 2). The streak record was optically scanned to determine numerical values for piston displacement. Then by differentiating twice and applying the equations of motion, a value for the vapor pressure causing the motion was obtained. The specific energy was determined by measuring with a time resolving optical pyrometer the specific energy absorbed at the center of a calorimeter plate positioned behind the target. This is measured before thermal diffusion alters the initial temperature distribution and before the calorimeter plate is destroyed by the piston motion. The graphite temperature was kept below 2000K due to its large heat capacity. The relation between the energy density measured at the calorimeter plate and the sample energy density is based upon electron transport calculations. The energy absorption profile is one dimensional and is determined by an electronphoton Monte Carlo Code (Halbleib and Vandevender 1974) prior to the experiment. See Figure 3 for the absorption profile. The discontinuities are due to the graphite- UO_2 interface.

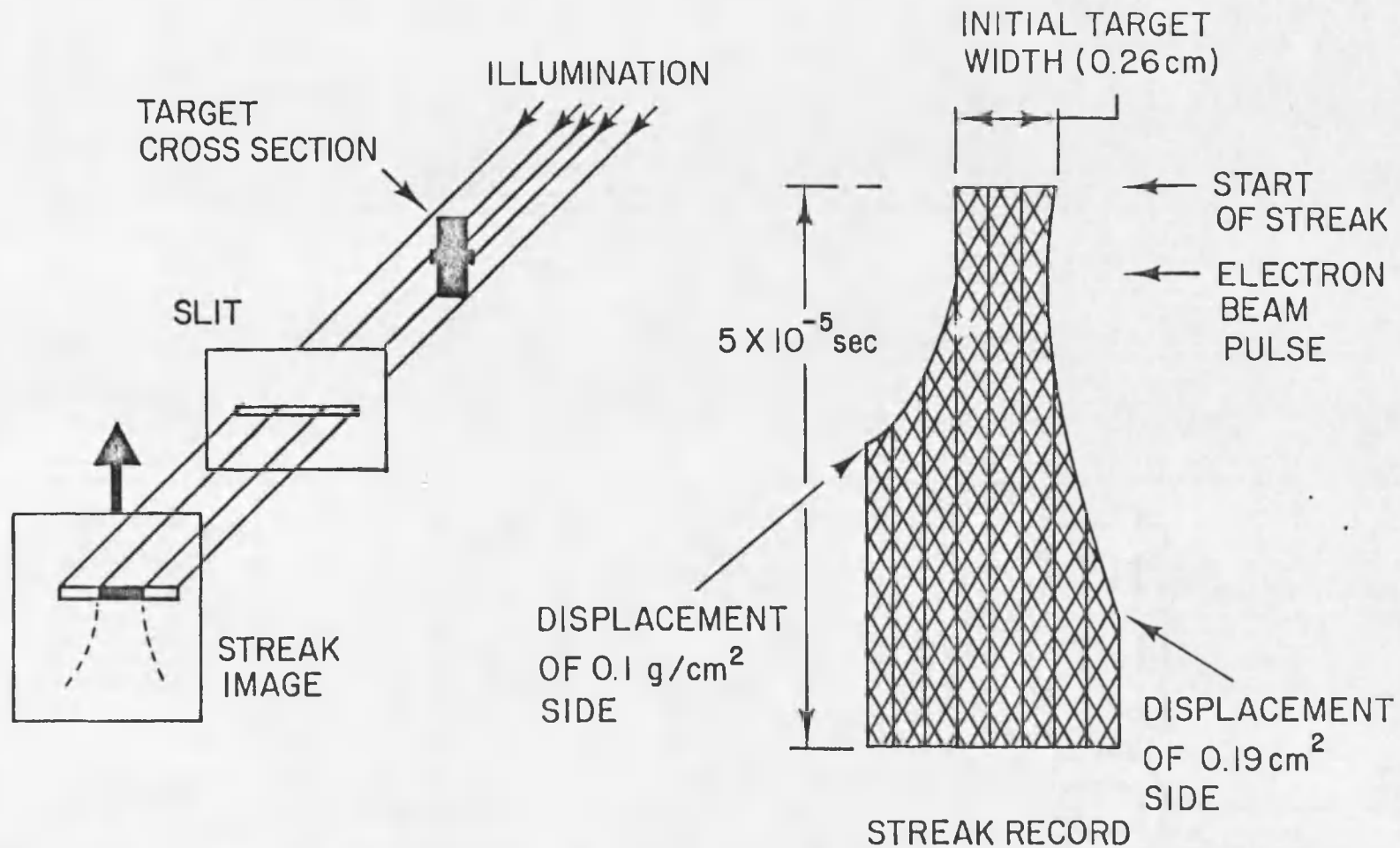


Fig. 2. Schematic Diagram of the Streak Recording System and an Example of the Experimental Record.

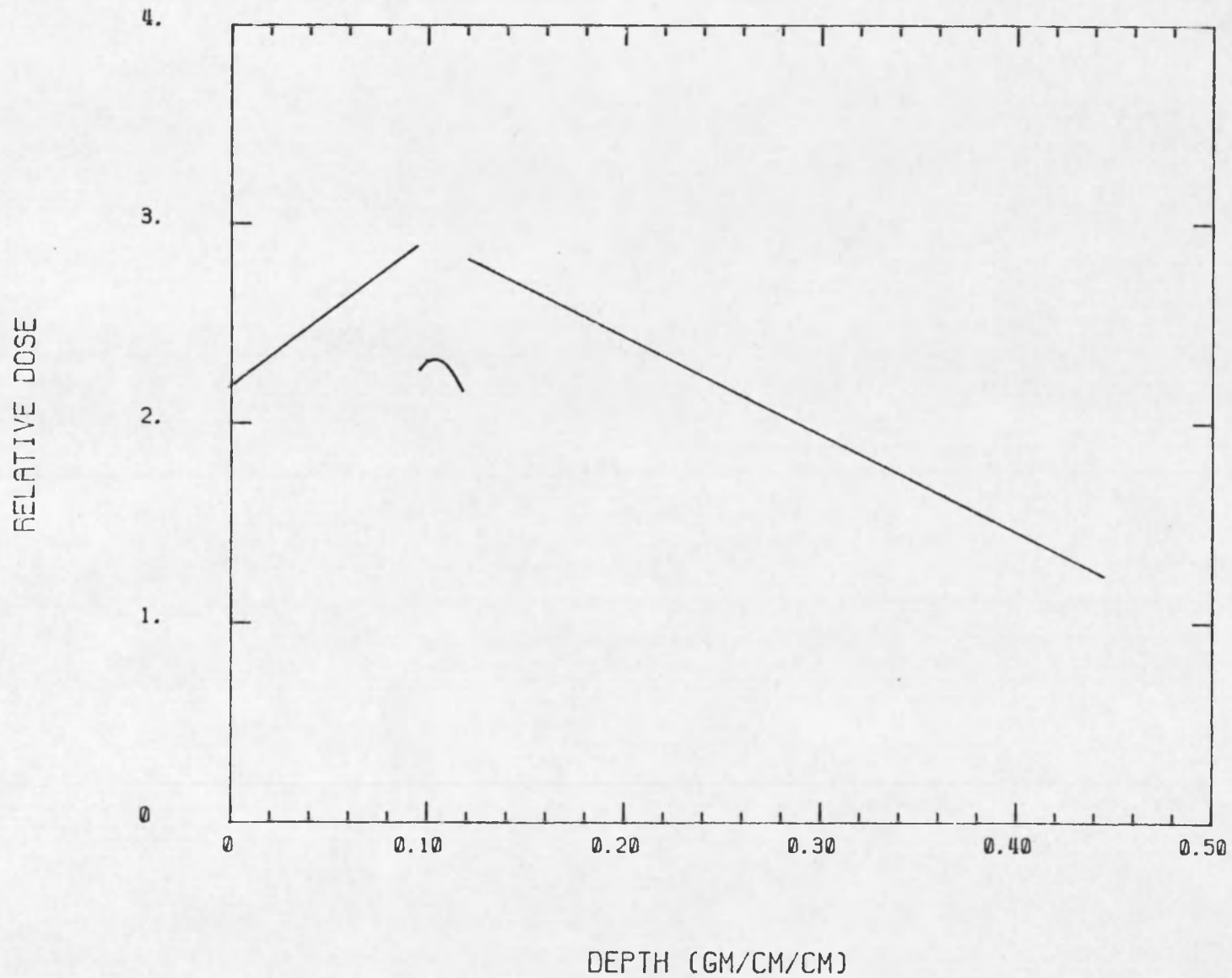


Fig. 3. Electron Energy Absorption Profile as a Function of Mass Depth

2.3 Experimental Results

Velocity profiles from five electron beam tests are shown in Figure 4. The curves are actually linear fits to the data points. These linear fits are used to determine the vapor pressure. Data points are plotted for the 2030 J/gm case and the 3030 J/gm case. The scatter was attributed to the finite resolution of the displacement photos. Benson (1977) notes that there is no negative curvature of the fit velocity profiles. Negative curvature would indicate a drop in vapor pressure during the experiment.

Each of the velocity profiles is offset from zero velocity; this curve offset is attributed to the transfer of momentum from the condensed phase sample material. Liquid motion is induced by violent thermal expansion of the liquid droplets in response to the absorbed electron energy. This forces a splashing of some liquid phase against the surface of the graphite container producing an intense but short duration loading. Other possible contributions listed are the presence of small volume fractions of material having higher volatility and a possible carbon-oxygen reaction.

The experimental data is plotted in Figure 5 and fit to a model which assumes the slope of the logarithm versus $1/(E-E_0)$ is constant. The data is listed in Table 1.

Comparisons of Benson's results to other EOS models have been made. In this paper, Benson used Menzies' and Ackerman's equations of state with two heat capacity models so that the comparison could be made in a pressure-energy format. The first model assumed a

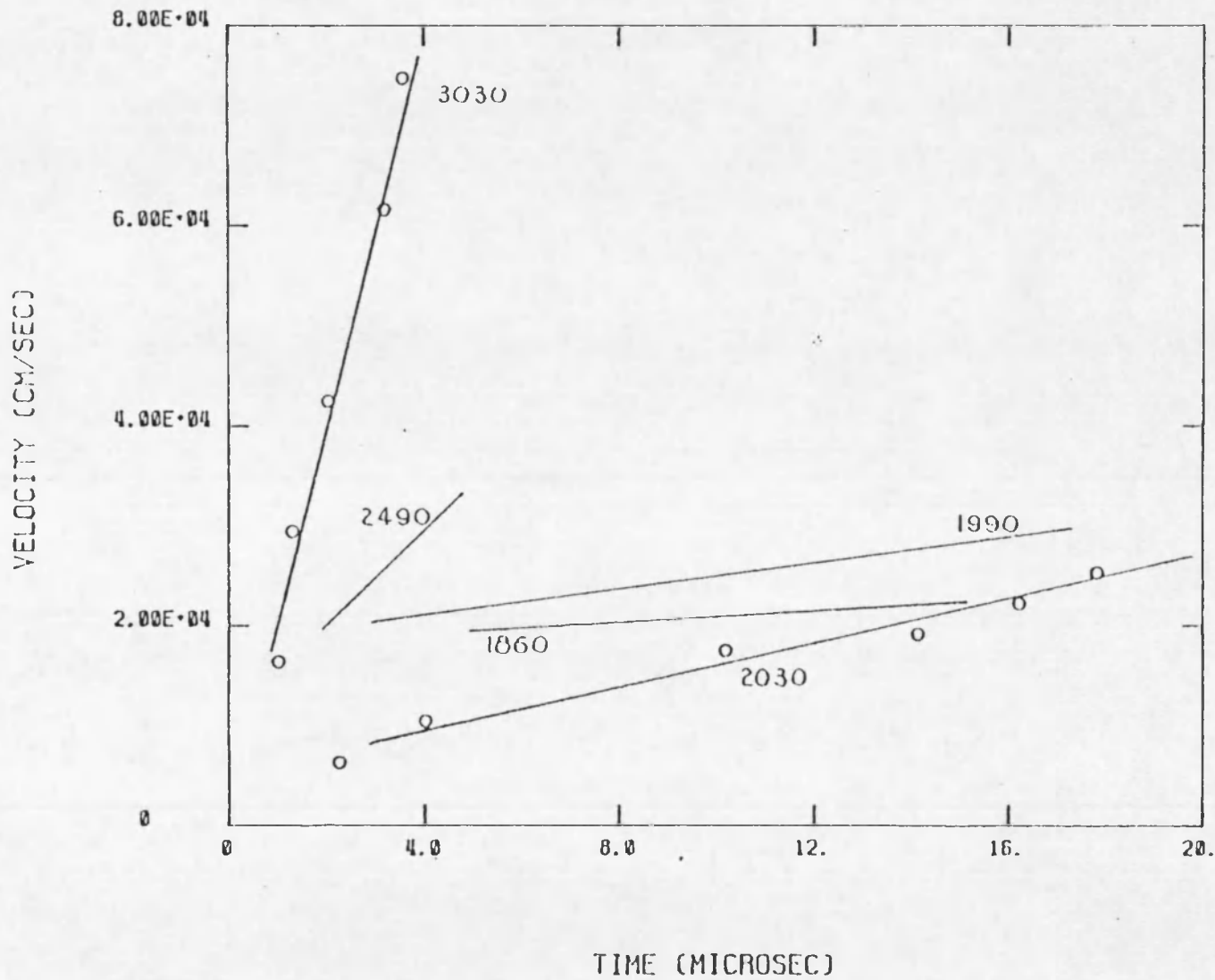


Fig. 4. Velocity as a Function of Time for Five Energy Pulses.

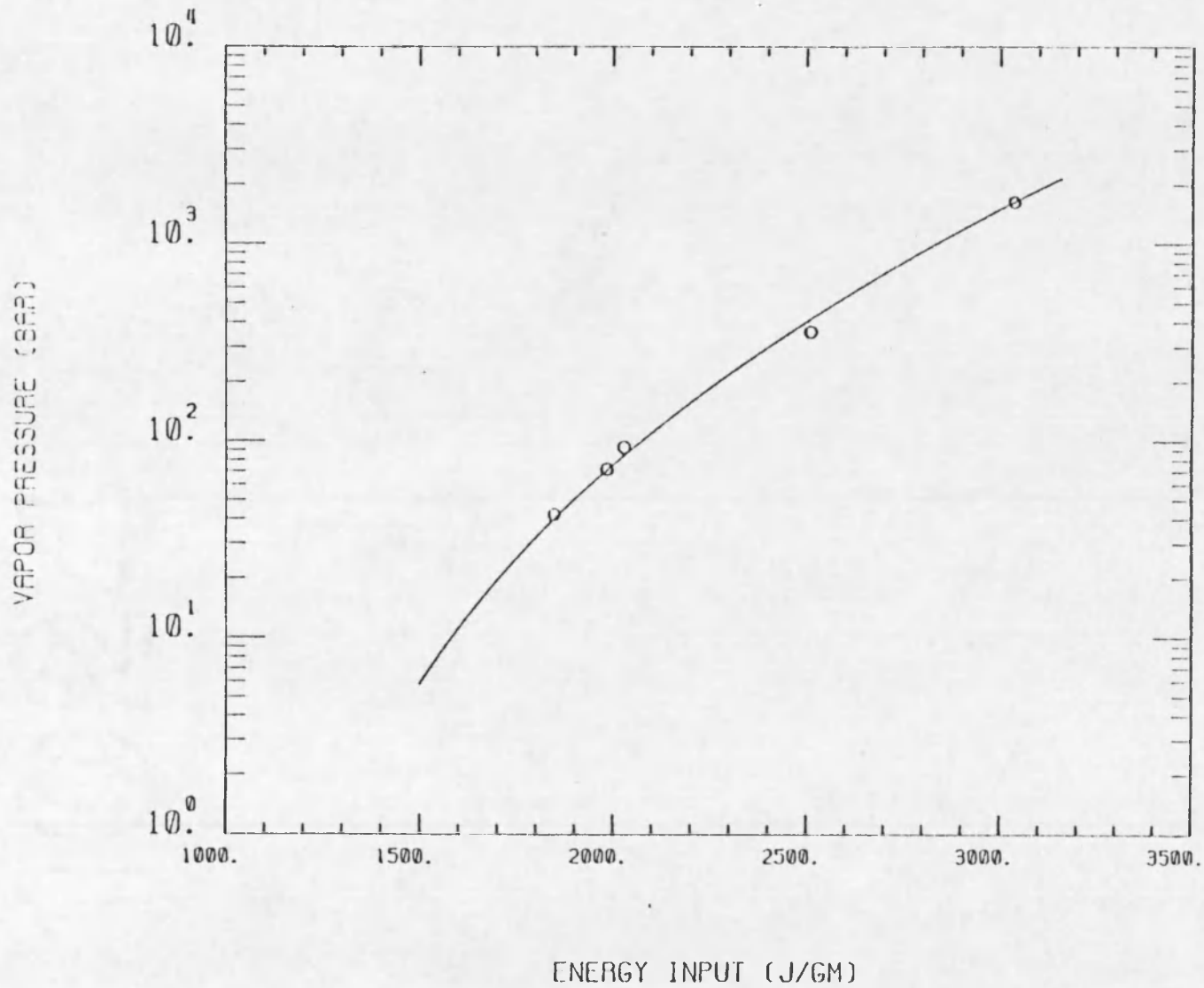


Fig. 5. Vapor Pressure as a Function of Internal Energy.

Table 1. Vapor Pressure as a Function of Specific Energy

<u>Energy (J/g)</u>	<u>Pressure (Bar)</u>
1860	43
1990	66
2030	96
2490	322
3030	1500

constant average heat capacity of 0.44 J/g K. The second model used measured values with an average heat capacity of 0.33 J/g K below melt and 0.50 J/g K above melt with a 276 J/g heat of fusion.

Using these heat capacity models with each of the two equations of state resulted in the four pressure-energy curves in Figure 6. Benson's data is also plotted in Figure 6. For a particular energy deposition, Menzies' EOS predicted a lower vapor pressure while Ackerman's EOS predicted a higher vapor pressure. The two equations appear to bound the vaporization experiment data when used with the above two heat capacity models.

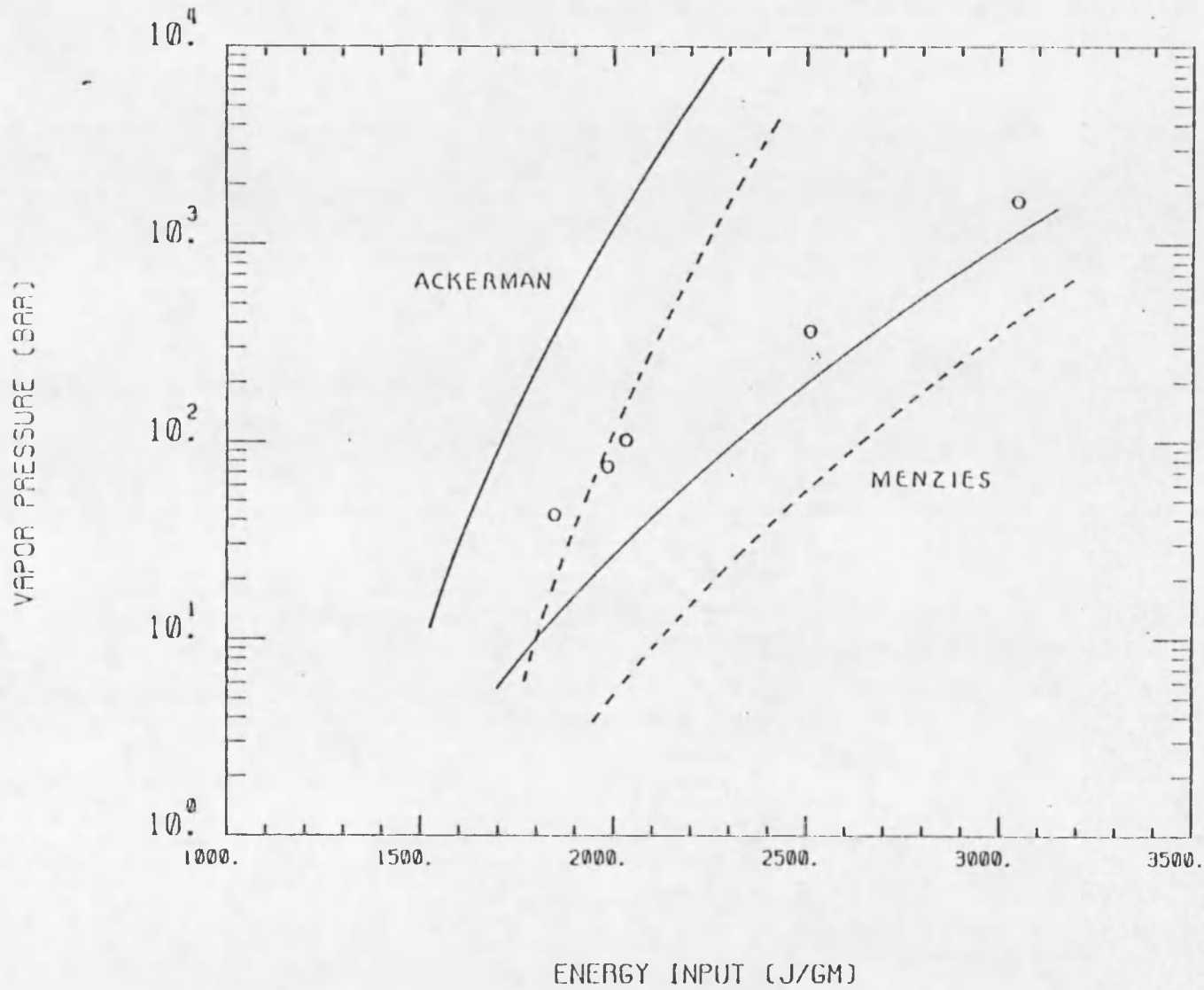


Fig. 6. Ackerman's and Menzies' EOS Plots Using Two Heat Capacity Models.

CHAPTER 3

THE FARA CODE

FARA (Ganapol 1977 and 1978) is designed to solve the finite difference equations arising from two component fluid flow. In this chapter, we will detail how the code works, including finite difference equations solved, solution algorithm, coding and benchmark problems. The following discussion will be for a one component model only.

The FARA code (Ganapol 1977 and 1978) solves the Eulerian fluid flow conservation equations in one dimension.

$$\frac{\partial \rho}{\partial t} + \frac{\partial (\rho u)}{\partial z} = 0$$

$$\frac{\partial (\rho u)}{\partial t} + \frac{\partial (\rho u^2)}{\partial z} = - \frac{\partial P}{\partial z}$$

$$\frac{\partial (\rho e)}{\partial t} + \frac{\partial (\rho e u)}{\partial z} = - \frac{P \partial u}{\partial z} + s(t)$$

where ρ = density

u = velocity

e = specific internal energy

P = pressure

$s(t)$ = source term

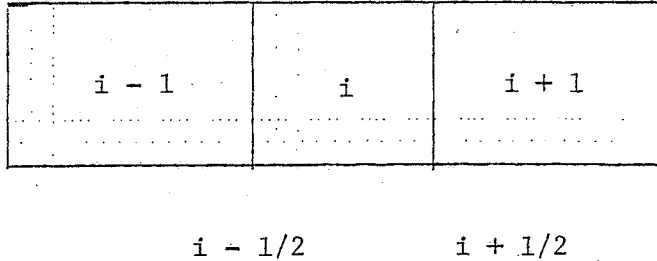
Coupled with the above equations is Benson's equation of state (Ostenson 1979).

$$P = 10 \times \text{EXP}(26.142 - 49729/T)$$

$$T = \Delta E / C_p + T_0$$

3.1 Numerical Methods

The above equations are formulated into finite difference equations which form a non-linear algebraic set for the field variables. The convective term in the continuity and energy balance equations are approximated by a full donor cell differencing scheme, while the momentum balance equation is approximated by a partial donor cell differencing scheme (Ganapol 1977). The mesh scheme is defined as



In the FARA code, the velocities are cell edged while all other field variables are cell centered. Superscripts refer to time dependence. Subscripts refer to spatial dependence. The continuity equations are rewritten as

$$\frac{\rho_i^{N+1} - \rho_i^N}{\Delta t} + \frac{1}{2\Delta z_i} \left[\rho_i^{N+1} \cdot (u_i^{N+1} + |u_i^{N+1}|) \right]$$

Mass

$$\left. \begin{aligned} & + \rho_{i+1}^{N+1} \cdot (u_i^{N+1} - |u_i^{N+1}|) - u_i^{N+1} \cdot (\rho_{i-1}^{N+1} + \rho_i^{N+1}) \\ & - |u_i^{N+1}| \cdot (\rho_{i-1}^{N+1} - \rho_i^{N+1}) \end{aligned} \right] = 0.0$$

where:

$$\bar{\Delta z}_i = 1/2 (\Delta z_i + \Delta z_{i+1})$$

Momentum

$$\frac{(\rho u)_{i+1/2}^{N+1} - (\rho u)_{i+1/2}^N + 1.0}{\Delta t \Delta z_i} (\rho u^2)_{i+1}^{N+1} - (\rho u^2)_i^{N+1}$$

$$+ \frac{\theta_i^{N+1}}{\bar{\Delta z}_i} \rho_{i+1}^{N+1} - \rho_i^{N+1} = 0.0$$

where:

$$(\rho u^2)_i^{N+1} = 1/2 \rho_i^{N+1} (u_{i+1/2} + u_{i-1/2})^{Y_{i+1}}$$

$$+ (u_{i-1/2} - u_{i+1/2}) |Y_i|^{N+1}$$

$$(\rho u^2)_{i+1}^{N+1} = 1/2 \rho_{i+1}^{N+1} (u_{i+3/2} + u_{i+1/2})^{Y_{i+1}}$$

$$+ (u_{i+1/2} - u_{i+3/2}) |Y_{i+1}|^{N+1}$$

$$\theta = \text{volume fraction} = 1.0$$

$$Y_i^{N+1} = 1/2 \cdot (u_{i+1/2} + u_{i-1/2})^{N+1}$$

$$Y_{i+1}^{N+1} = 1/2 \cdot (u_{i+3/2} + u_{i+1/2})^{N+1}$$

$$\rho_{i+1/2}^{N+1} = d_i \rho_{i+1}^{N+1} + c_i \rho_i^{N+1}$$

$$\theta_{i+1/2}^{N+1} = d_i \theta_{i+1}^{N+1} + c_i \theta_i^{N+1}$$

$$c_i = \frac{\Delta z}{\Delta z_i + \Delta z_{i+1}} \quad d_i = \frac{\Delta z_{i+1}}{\Delta z_i + \Delta z_{i+1}}$$

Energy

$$\begin{aligned} & \frac{(\rho e)_i^{N+1} - (\rho e)_i^N}{\Delta t} + \frac{1}{\Delta z_i} \left[(\rho e u)_{i+1/2}^{N+1} - (\rho e u)_{i-1/2}^{N+1} \right] \\ & + \theta_i^{N+1} \left[P_i^{N+1} + P_{i+1}^{N+1} \right] \cdot \frac{1}{\Delta z_i} \left[u_{i+1/2}^{N+1} - u_{i-1/2}^{N+1} \right] \\ & - \rho_i^{N+1} s(t)^{N+1} = 0.0 \end{aligned}$$

where:

$$\begin{aligned} (\rho e u)_{i\pm 1/2}^{N+1} = & 1/2 \left\{ \left[(\rho e)_{i\pm 1} + (\rho e)_i \right]^{N+1} \cdot u_{i\pm 1/2}^{N+1} \right. \\ & \left. \pm \left[(\rho e)_{i\pm 1} - (\rho e)_i \right]^{N+1} \cdot |u_{i\pm 1/2}^{N+1}| \right\} \end{aligned}$$

s(t) = time dependent source input

The FARA code employs the multivariate Newton-Raphson technique (Nakamura 1977) for its solution algorithm. An iterative procedure is defined for each cell i , such that convergence to the

solution of the nonlinear equations is effected through an approach along the gradient of the solution surface mapped out by the variables in the equation set. The calculational scheme moves from left to right, each cell taken in order. The Newton-Raphson iteration at each cell is termed an inner iteration while a sweep through the mesh grid constitutes one outer iteration.

For any particular cell i , the knowledge of the downstream advanced time variable is required, which is unknown. To bypass this problem, these quantities are assumed to have the values of the previous outer iteration.

In the solution scheme for a single component, the finite difference equations describing the flow are numbered as follows:

- F(1) = mass continuity
- F(3) = momentum balance
- F(7) = pressure correlation
- F(9) = energy balance
- F(12) = temperature correlation

If the above equations were solved simultaneously, it would be considered an implicit solution. However, it is possible to solve an equation at the conclusion of each outer iteration. This is considered an explicit solution method, optioned by input switches. One advantage of this is a reduction in computer costs.

In the Newton-Raphson solution algorithm, the k th approximation to the true value is obtained by

$$x^k = x^{k-1} - \left[\frac{\partial F}{\partial x} (x^{k-1}) \right]^{-1} \cdot \bar{F}(x^{k-1})$$

where x^k = the array of field variables

$\bar{F}(x^{k-1})$ = equation residues

$[\underline{F}'(x^{k-1})]^{-1}$ = inverted Jacobian matrix

The solution algorithm requires the inverse of the Jacobian matrix.

The elements of the Jacobian matrix for this problem

$$J = \begin{array}{ccc} \frac{\partial F_1}{\partial x_1} & \frac{\partial F_1}{\partial x_3} & \frac{\partial F_1}{\partial x_9} \\ \frac{\partial F_3}{\partial x_1} & \frac{\partial F_3}{\partial x_3} & \frac{\partial F_3}{\partial x_9} \\ \frac{\partial F_9}{\partial x_1} & \frac{\partial F_9}{\partial x_3} & \frac{\partial F_9}{\partial x_9} \end{array}$$

are determined from the equations defining the residuals. Convergence is satisfied when the kth approximation is within some specified value of the k-1 approximation. Each variable has its own error bounds with a possible 20 inner iterations allowed per mesh cell.

On a cell by cell basis, the calculational scheme is

1) determination of equation residuals, 2) calculational of the Jacobian matrix, 3) inversion of Jacobian, 4) determination of advanced time variable values and 5) repeat until convergence.

The above procedure is repeated for each cell until an outer iteration is completed. A time step is completed when all of the outer iterations are completed.

3.2 Benchmarking

As previously mentioned, FARA was conceived as a test base. As such, the FARA code was tested and benchmarked (Ganapol 1977 and 1978). For the UO_2 experiment analysis, several modifications were

necessary, resulting in further testing. The modifications include an energy source input and boundary motion. Benchmark problems are a means of determining code accuracy. These and other benchmark problems will now be discussed.

Energy Source Input

This was one of the changes necessary to properly analyze the UO_2 equation of state experiment. Based on the energy pulse data supplied by Benson (1977), the energy term was Gaussian in time with a 0.6 microsec FWHM duration. From this it was determined

$$s(t) = \frac{A}{\sigma\sqrt{2\pi}} \text{EXP} \left(-1/2 \frac{(t-\mu)^2}{\sigma^2} \right)$$

where $s(t)$ = time dependent source term

A = total energy deposited (J/g)

σ = standard deviation (sec)

$$= \frac{\text{FWHM}}{2\sqrt{2 \cdot \ln 2}}$$

μ = mean = 3σ (sec)

This term was added to the energy balance equation.

In order to test the source input equation, a no-flow, energy addition problem was solved analytically using the ideal gas law for an EOS. The solution to the problem is

$$(e-e_0) = \frac{A}{2} \text{erf} \frac{\mu}{\sqrt{2\sigma}} - \text{erf} \frac{\mu-t}{\sqrt{2\sigma}}$$

for $\mu > t$

$$(e-e_0) = \frac{A}{2} \text{erf} \frac{\mu}{\sqrt{2\sigma}} + \text{erf} \frac{t-\mu}{\sqrt{2\sigma}}$$

for $t > \mu$

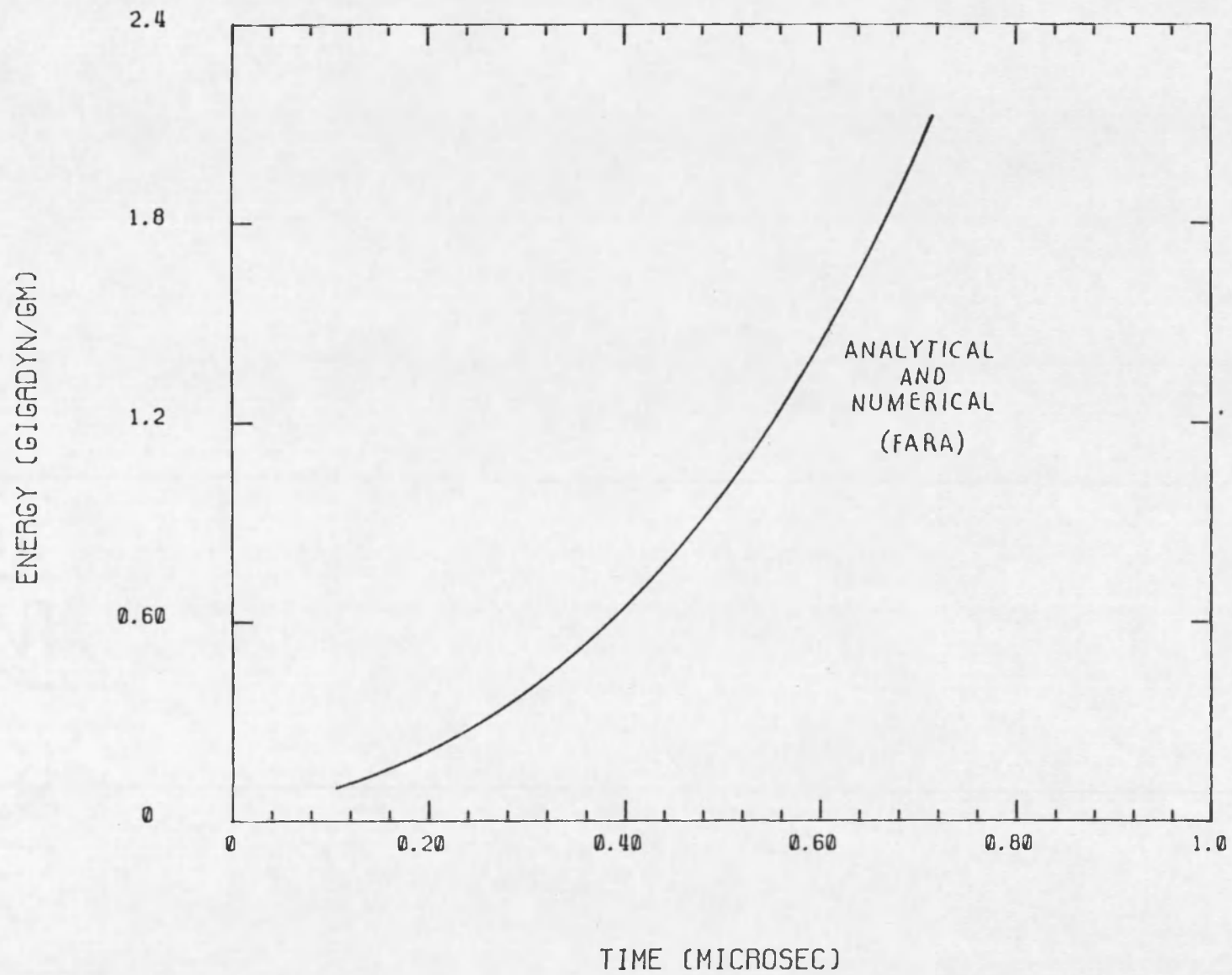


Fig. 7. Energy Input Benchmark

The test problem had a 500 J/g peak energy source. The time step was 5 nsec and there were 140 time steps. Analytical and numerical results are plotted in Figure 7 for $\mu > t$ only. There is excellent agreement between FARA'S numerical results and those of the analytical solution.

Frictional Flow

This is a duct flow problem that examines the momentum loss due to friction at the walls. This problem was originally benchmarked for two components (Ganapol 1977 and 1978) but is repeated here. The purpose of this problem is to provide an overall check on code integrity, since the frictional loss term is not used in the EOS analysis.

The initial fluid velocity was 100 cm/sec with a frictional coefficient f of 1000 (g/cm^4). The analytical solution for an incompressible fluid is

$$u = 1 + \frac{u_0}{\rho} \frac{f t}{u_0 f t}$$

For this problem, the density was $1.3\text{E}-03 \text{ g}/\text{cm}^3$, the time step 1 nsec with a total of 50 time steps. The analytical and numerical velocities are shown in Figure 8. The code results are somewhat high but within a reasonable error bound of 1 percent. The numerical solution appears to be 0.5 nsec faster than the analytical.

Explicit vs Implicit

This is a comparison of an explicit solution to an implicit solution for an identical problem. The purpose was to determine any differences in the two methods. A frictional flow problem was selected.

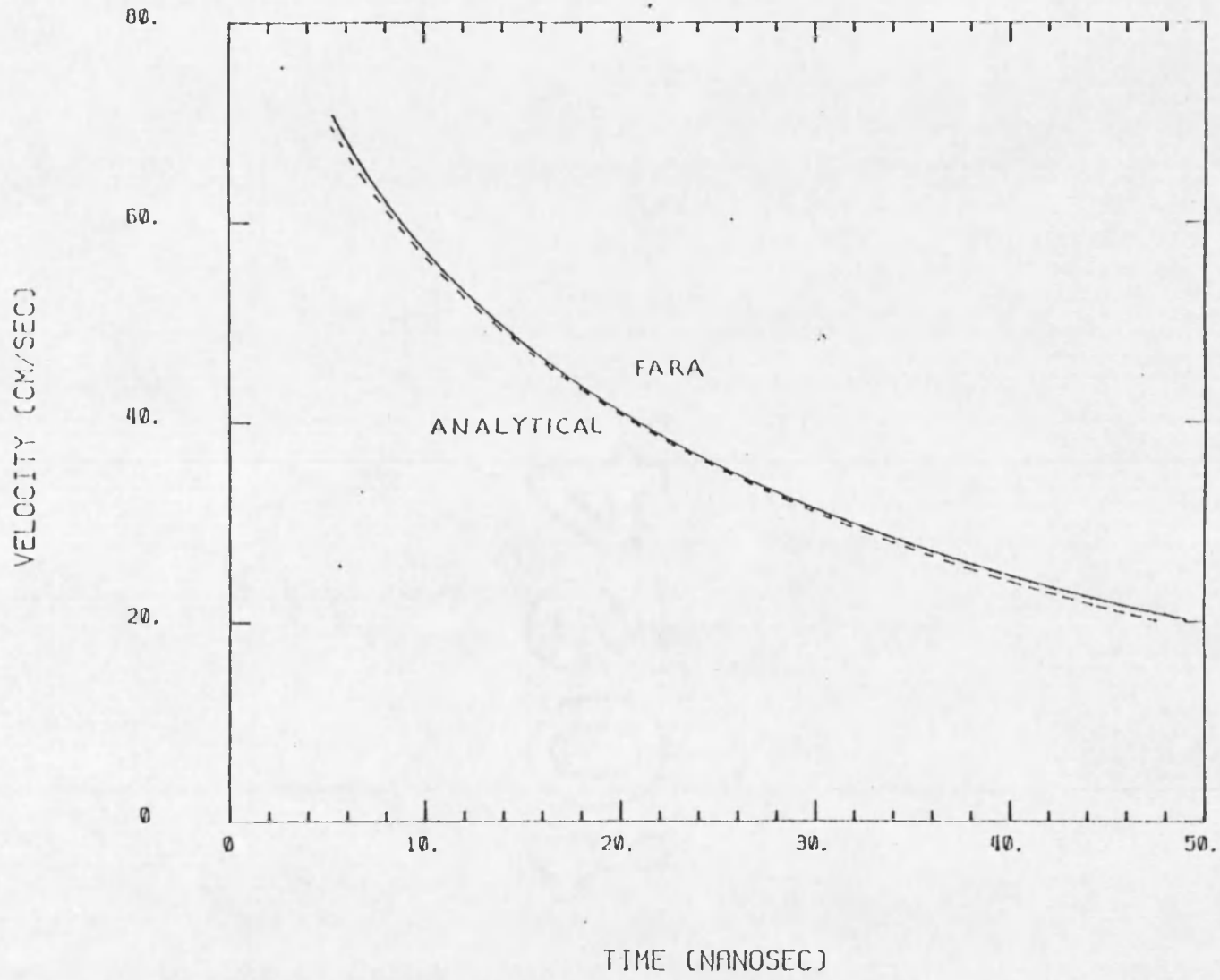


Fig. 8. Frictional Flow Benchmark

In this case, the initial velocity was 100 cm/sec with a frictional coefficient of 100. The time step was 1 nsec with a duration of 200 nsec. The results from the two cases were identical to four decimal places.

Heat Transfer

A quiescent two component heat transfer problem was chosen for a detailed examination of the code's heat transfer capabilities between two fluids, although only a single fluid is being modeled for the UO_2 experiment. The analytical solution is of the form

$$T_1 = \frac{1}{1 + \frac{\rho_2 \beta_1}{\rho_1 \beta_2}} \left[T_{10} + \frac{\rho_1 \beta_2}{\rho_2 \beta_1} (T_{20} + (T_{10} - T_{20}) e^{-\alpha t}) \right]$$

$$\alpha = h(\beta_1 \rho_2 + \rho_1 \beta_2)$$

$$T_1 = \beta_1 E_1 \cdot T_2 = \beta_2 E_2$$

h = heat transfer coefficient

T_{10}, T_{20} = initial temperature

$$T_{10} = 4000k, T_{20} = 1200K$$

In the implicit solution, the temperature deviated substantially from the exact solution. See Figure 9. The deviation is caused by numerical mass diffusion resulting in an incorrect pressure determination. When the pressure was found explicitly, the exact solution was reproduced. For both the implicit and explicit solutions three outer iterations have been performed. The number of outer iterations have been performed. The number of outer iterations was

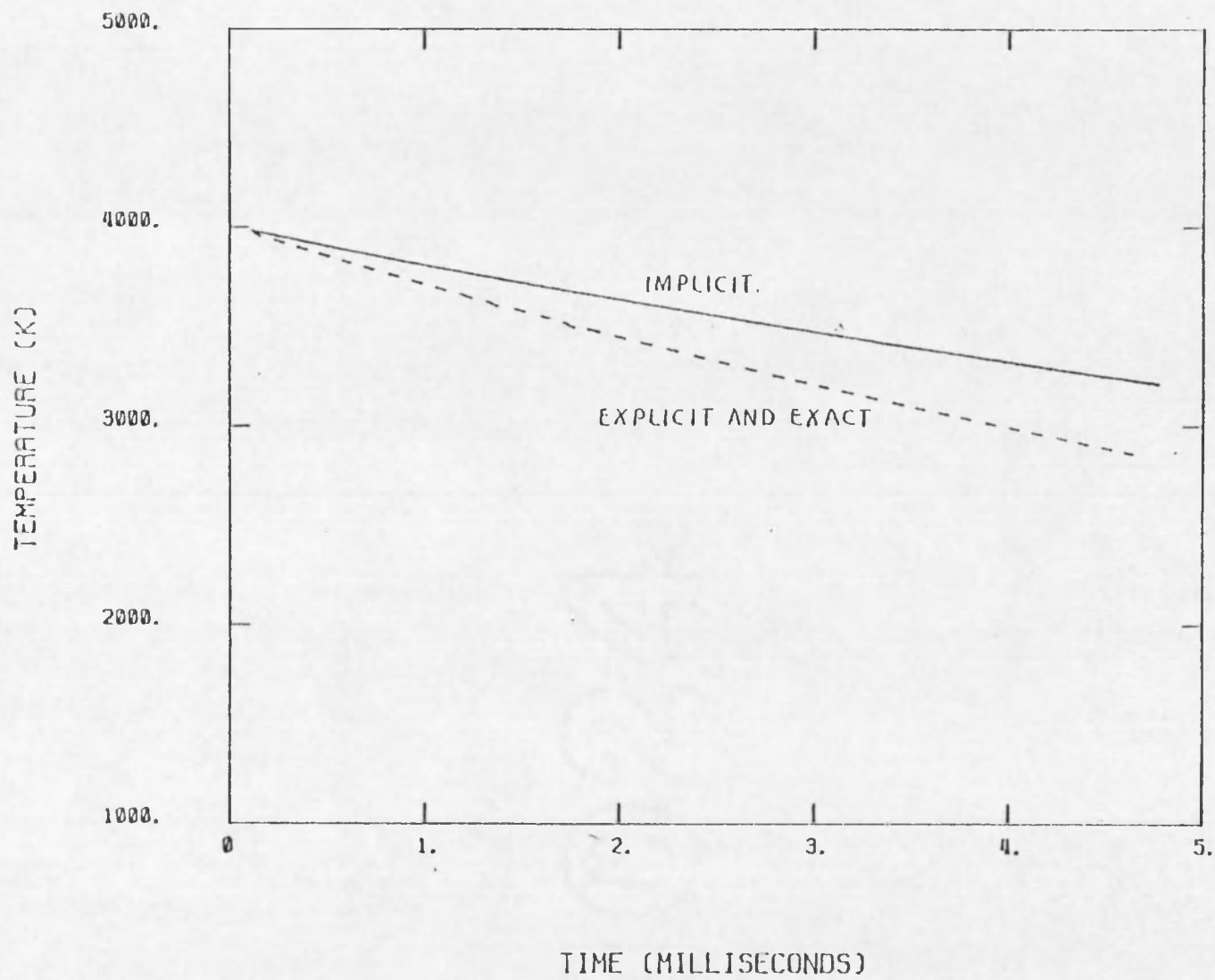


Fig. 9. Heat Transfer Benchmark

altered to determine if this had any effect. After 30 outer iterations, the implicit solution approached the analytical and the explicit remained unchanged. Thus an explicit formulation when heat transfer is dominant will provide a more accurate result.

Shock Tube

A one component shock tube problem was used as a benchmark to be sure that FARA contains no algorithmic inaccuracies. The analytical solution (Harlow and Amsden 1971) was programmed into FARA and can be accessed through an input option. The physical situation modeled is a diaphragm rupture between two perfect gasses at different densities. Resulting flow is from left to right (higher density to lower). The time step was 10 microseconds and a comparison of analytical to numerical results was made at 0.5 msec. Figure 10 is a plot of density versus time for the shock tube problem. Numerical smoothing causes a loss of detail between the contact surface and the shock front. The approximation to the rarefaction is reasonably accurate.

Boundary Motion

By far the most difficult modification made to the FARA code was the addition of an expansion capability. Many ideas were not feasible because of the necessary inversion of the Jacobian matrix in the solution algorithm. The concept chosen focuses on the expansion of a 'ghost' cell due to a pressure gradient and fluid momentum. Originally the 'ghost' cell existed for boundary conditions

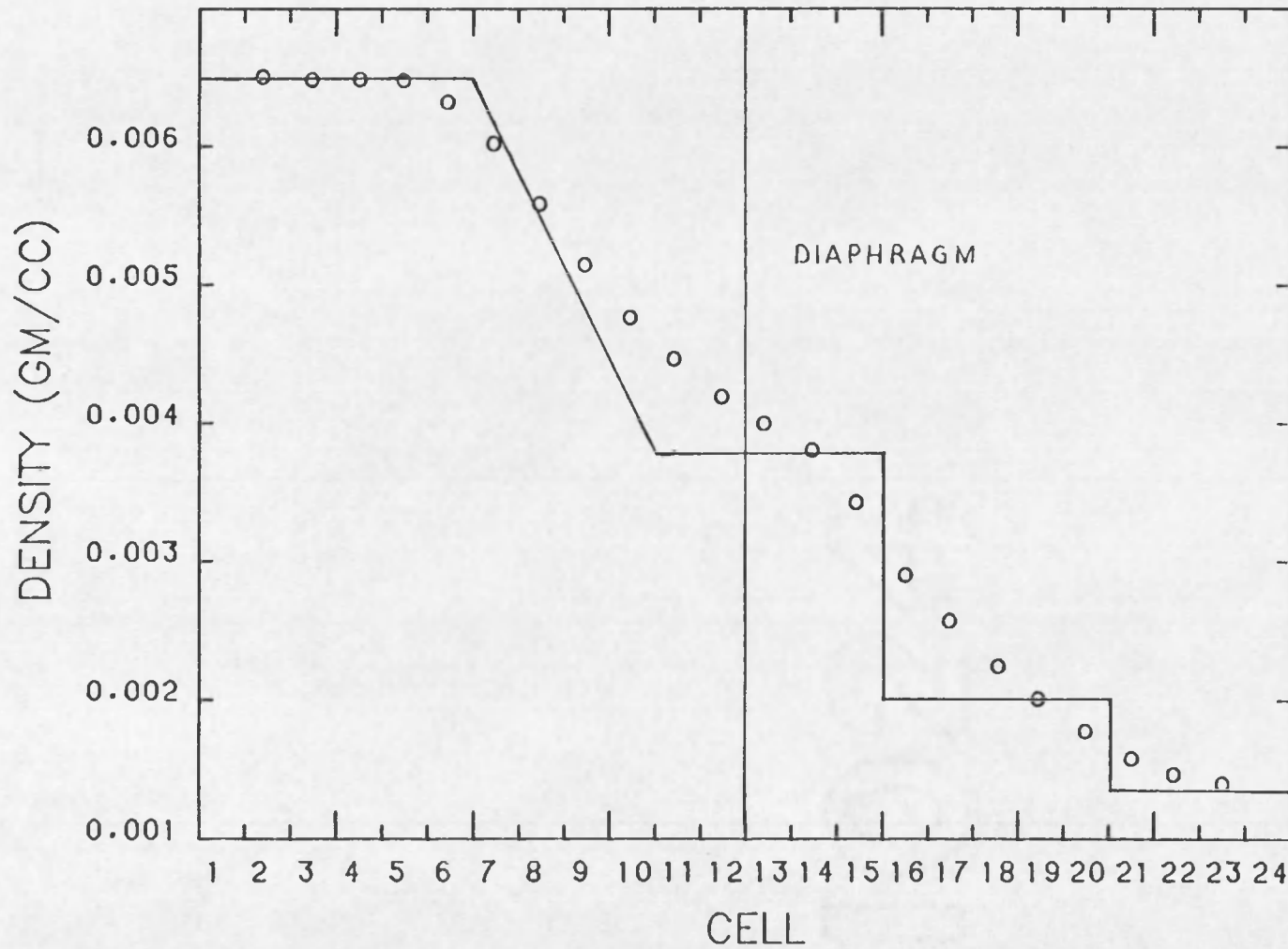


Fig. 10. Shock Tube Benchmark

(Ganapol 1977 and 1978). It was then modified to account for volume expansion.

Calculations for boundary motion begin at the conclusion of all the outer iterations. The concept is divided into three phases. The first phase is an accounting of mass and energy flowing into the expansion cell. The second phase is the actual expansion. An increase in cell volume is caused by a positive pressure gradient. An acceleration term is calculated based on the pressure gradient and fluid momentum. From the acceleration, we obtain piston velocity and displacement. The third phase entails determination of the effect of the displacement on the field variables in the cell.

A rarefaction problem was chosen for the benchmark analysis. Here the piston was given a constant velocity of 200 cm/sec. The fluid density was $1.3E-03$ g/cm³ and a perfect gas was assumed initially at 273K. The analytical solution for this rarefaction is plotted with numerical results in terms of density vs distance in Figure 11. In a rarefaction, the fluid is described by three regions. Region I is outside the rarefaction, Region II is the rarefaction wave and Region III is the undisturbed fluid. For a piston withdrawing to the right, the analytical solution for each region is (Harlow and Amsden 1971).

Region I

$$C = C_0 \frac{-\gamma - 1}{2} u_p$$

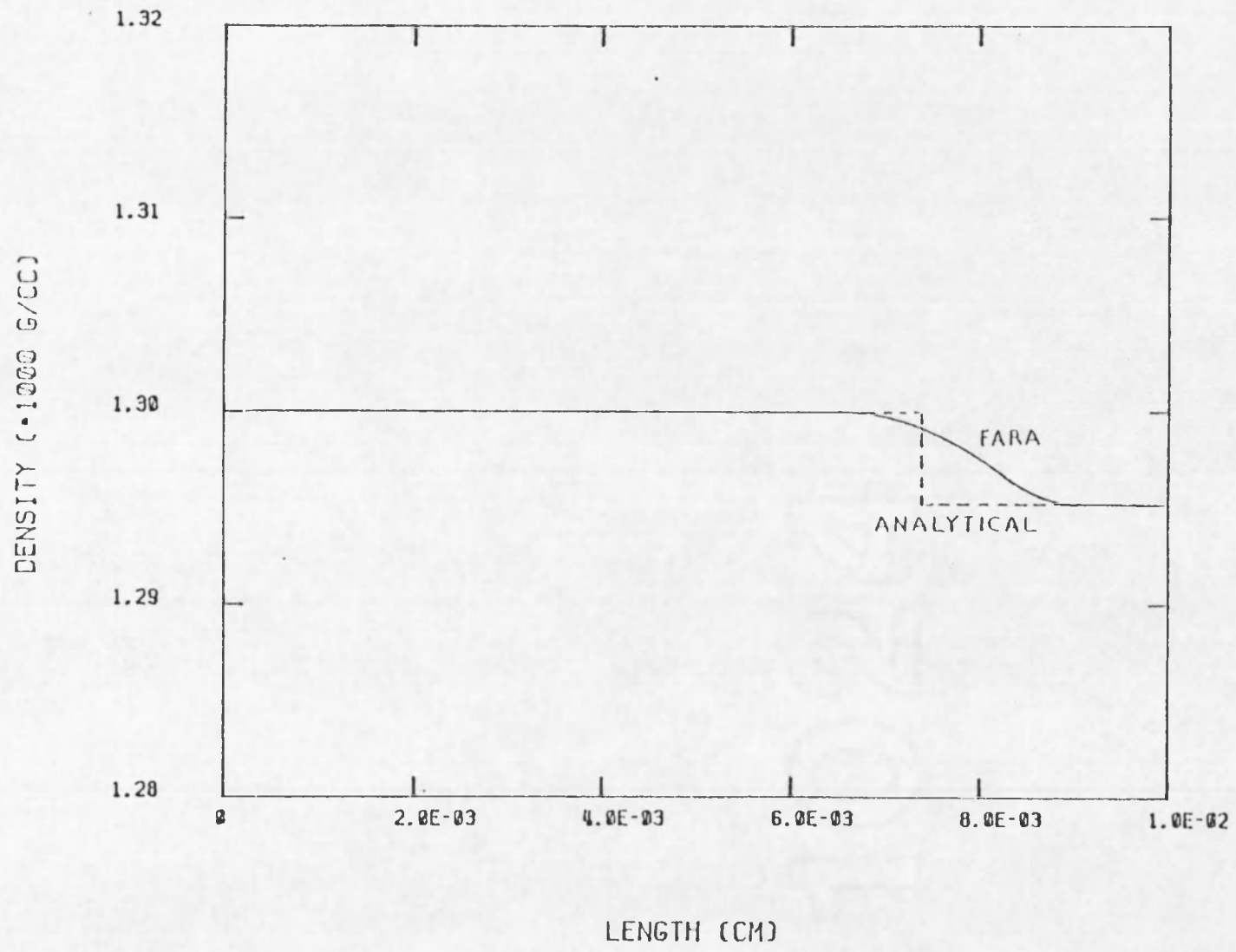


Fig. 11. Rarefaction Benchmark

Region II

$$c = \frac{\gamma-1}{\gamma+1} \left(\frac{-x}{t} + \frac{2c_0}{\gamma-1} \right)$$

Region III

$$c = c_0$$

and for any region

$$\rho = \rho_0 (c/c_0)^{2/(\gamma-1)}$$

The results are encouraging. FARA smoothes out the rarefaction wave (Region II) and maintains integrity in Regions I and III.

CHAPTER 4

NUMERICAL ANALYSIS

This chapter will focus on a discussion of experimental and numerical results of the UO_2 vapor pressure experiment.

4.1 Results

Numerical velocities calculated using Benson's EOS are compared to the experimental velocity fits for three energy pulses in Figures 12-14. The slopes of the experimental fit lines are used to determine the acceleration and consequently the vapor pressure, in the experimental analysis performed by Benson (1977). Recall that the offset of the experimental results is attributed to fluid impacting on the piston face.

For the 1860 J/g and 1990 J/g pulses, the slope of the numerical case matches closely with the slope of the experimental fit line. The obvious difference in each case is due to the offset of the experimental fit lines. The 2030 J/g pulse results are not as close as the two previous cases. There is a detectable difference in slope, indicating different vapor pressures.

4.2 Discussion

The objective of this thesis was to verify the results of the UO_2 experiment performed at Sandia. To do this, the hydrodynamics code FARA was employed which utilized the equation of state attributed

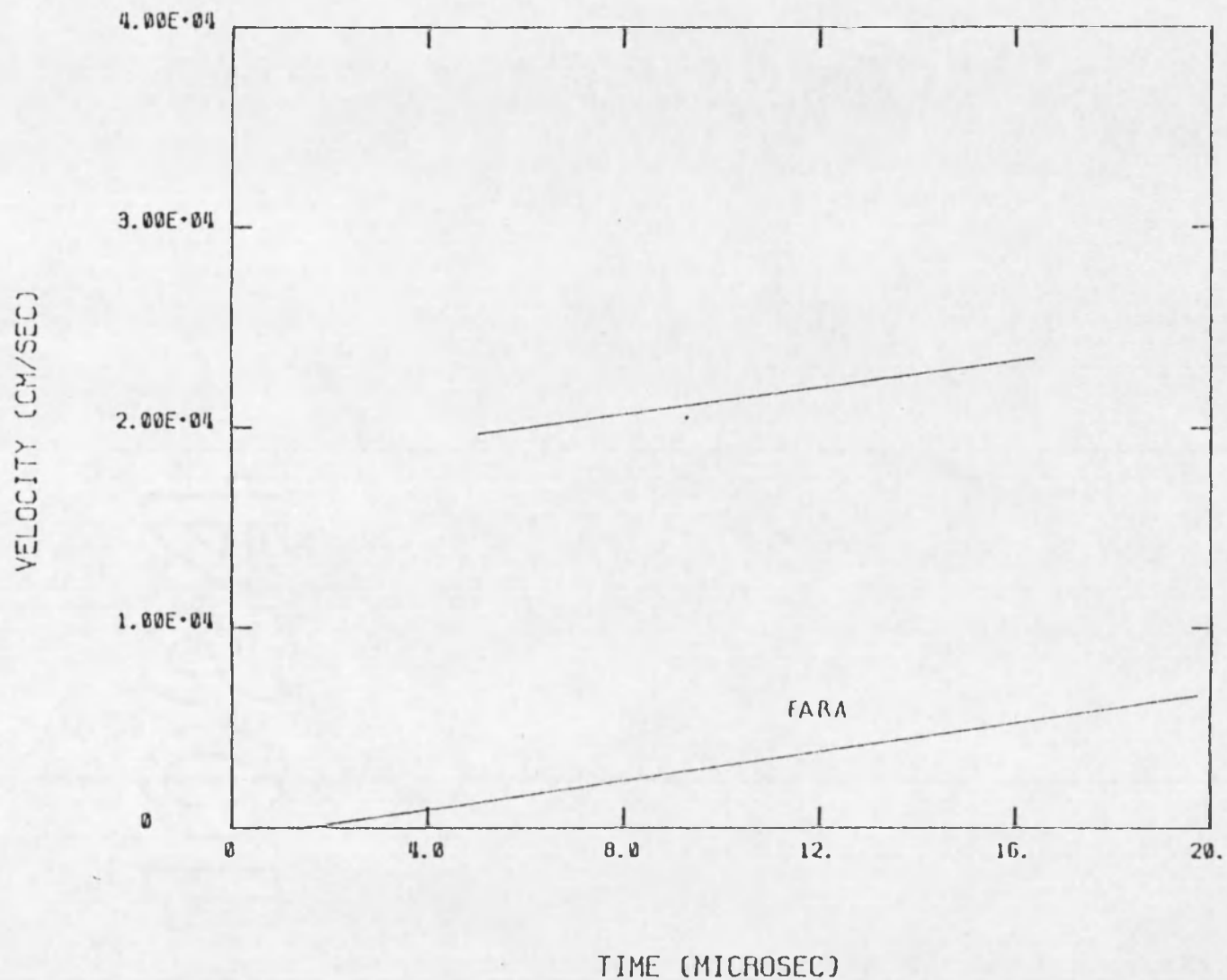


Fig. 12. Comparison of Experimental Fit to Numerical Results for the 1860 J/g Energy Pulse.

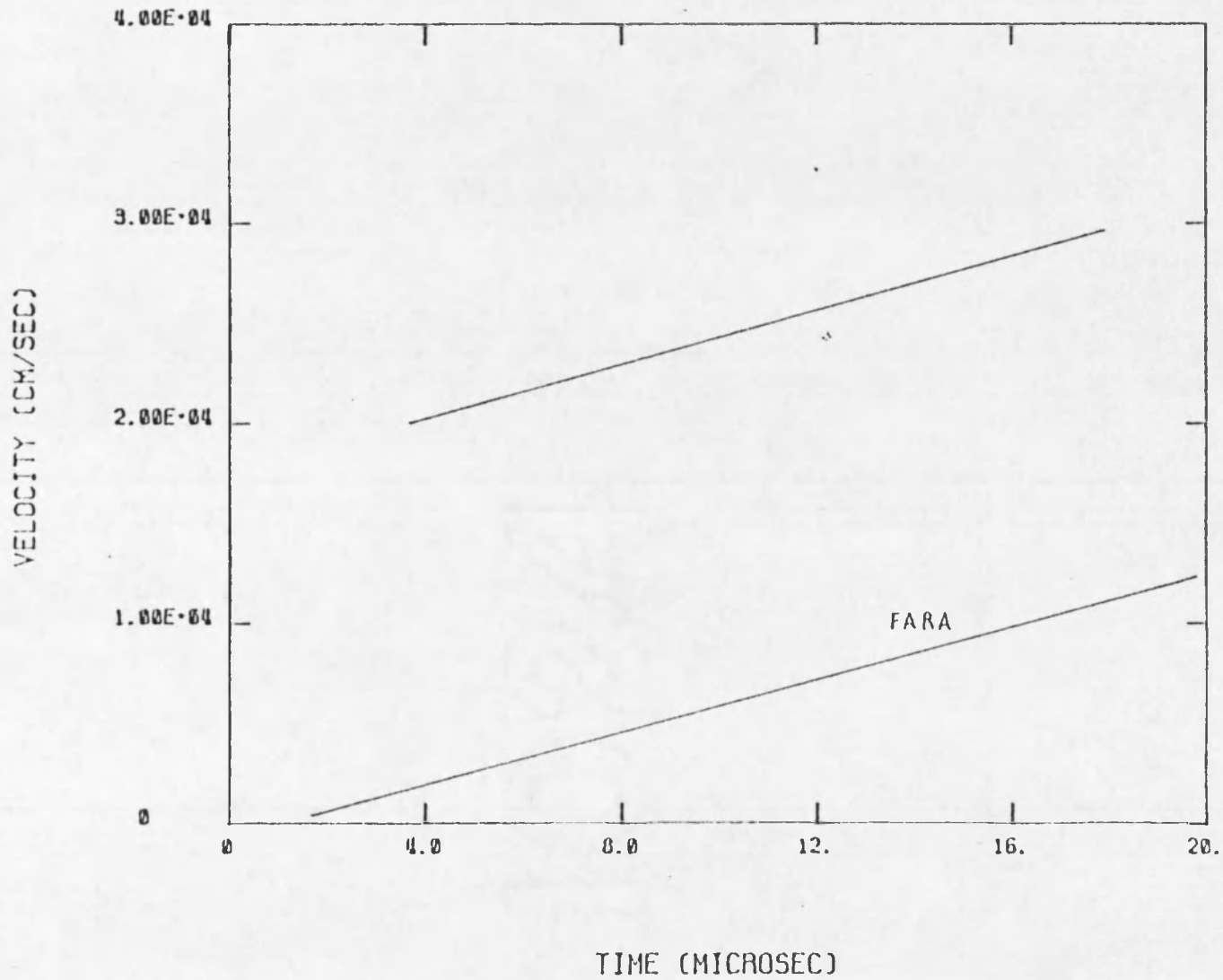


Fig. 13. Comparison of Experimental Fit to Numerical Results for the 1990 J/g Energy Pulse.

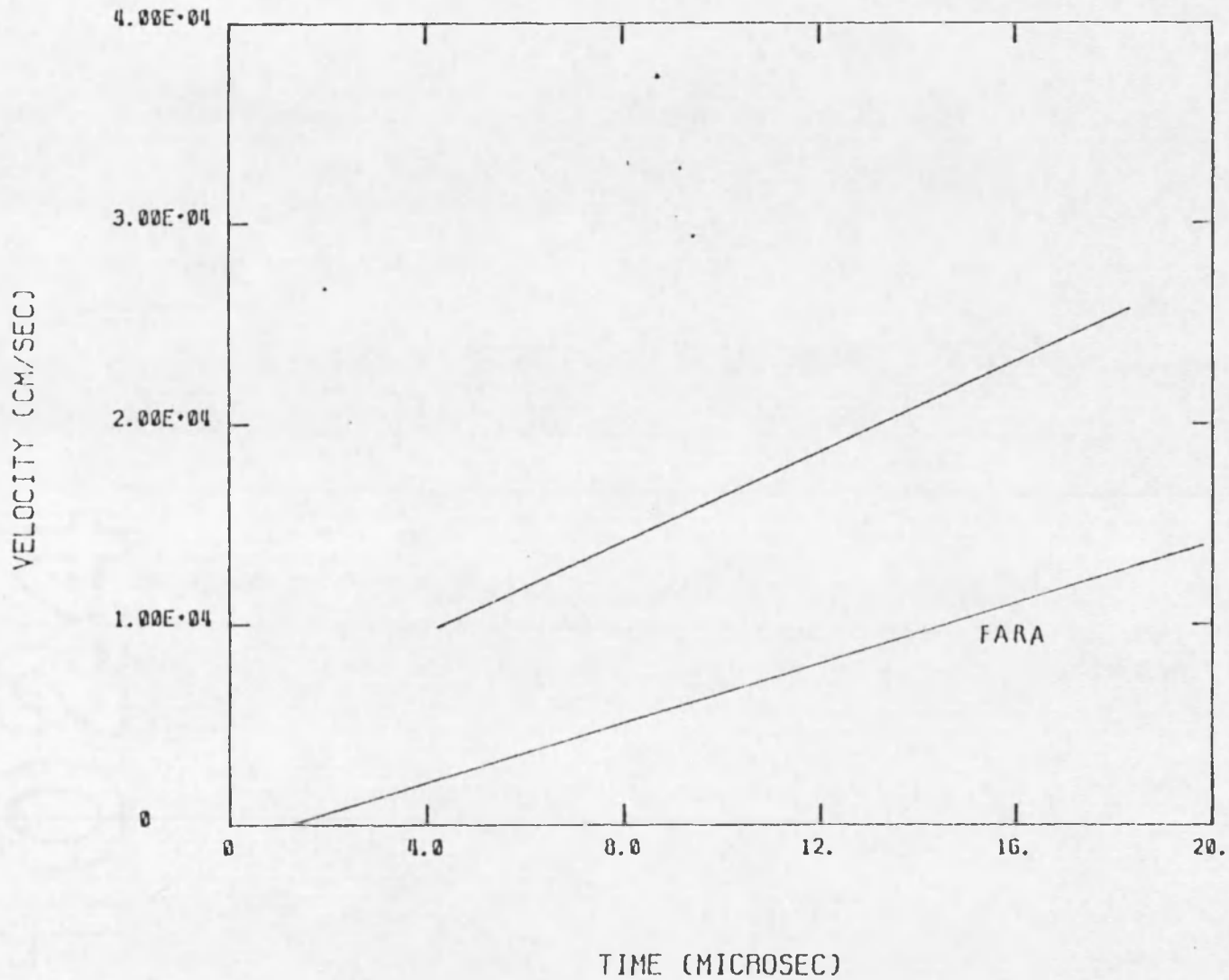


Fig. 14. Comparison of Experimental Fit to Numerical Results for the 2030 J/g Energy Pulse.

to Benson. Ostensen used the pressure-energy relationship determined by Benson to formulate the UO_2 equation of state. The relationship assumes the slope of the logarithm of vapor pressure versus inverse specific energy is constant. In order to obtain a pressure-temperature format, a heat capacity model had to be added.

There are three accepted heat capacity evaluations in use (Benson 1977). The first model assumes a constant average value of 0.44 J/g K over the entire temperature range from 1000K to 6000K. This is the heat capacity form of Menzies EOS. The second model is based on static measurements taken up to 3500K. Above 3500K, the heat capacity is assumed constant with a value of 0.5 J/g K. This model also assumes a 276 J/g heat of fusion. There is a large increase in the heat capacity as the temperature approaches the melting temperature. This rise in heat capacity has been attributed to oxygen Frenkel defect formation. The time scale for the effect of the Frenkel formation is much greater than the 20 microseconds required for the UO_2 experiment and accordingly this effect is discounted by Benson. This leads to a third model, a variation of the second without the effect of the Frenkel defect formation. The third model is based on extrapolated static data below 1500 K. This model has a 0.33 J/g K heat capacity below melt, a 0.50 J/g K value above melt with a 276 J/g heat of fusion. All three models are used by FARA to analyze the experiment.

Benson's analysis is based on the linear fit to the data points. Since the slope of the velocity is assumed to be proportional

to the vapor pressure, a change in slope will indicate a change in vapor pressure. His conclusions from this are that the vapor pressure is independent of expansion volume. This implies that the vapor pressure is constant throughout the volume, as opposed to the presence of pressure gradients.

On the surface, it would appear that the numerical results bear out Benson's hypothesis. Taking a closer look, this is not the case. The spatial energy deposition for the code's energy input is constant. This does not compare to the actual spatial deposition of Figure 3. The addition of a comparable spatial energy deposition would cause a more rapid initial acceleration followed by a gradual leveling of the velocity profile. Numerical results from the FARA code show definite pressure gradients, even though the slope of the velocity profiles are similar to the experimental fit. In FARA, piston velocity is a function of the final cell pressure. Extrapolating this to the experimental results, it would seem that pressure gradients exist in the UO_2 sample and the velocity of the piston is a function of the vapor pressure in the immediate region of the piston face. If this is the case, it is not possible to predict the vapor pressure of the sample from the velocity profile.

In his analysis of the UO_2 data, Benson attributed the scatter to the finite resolution of the displacement photos. One will notice that the 'scatter' has the same oscillatory pattern for both pulses in which actual data is shown. In a previous experiment with gold, the same oscillatory pattern was present (see Figure 15).

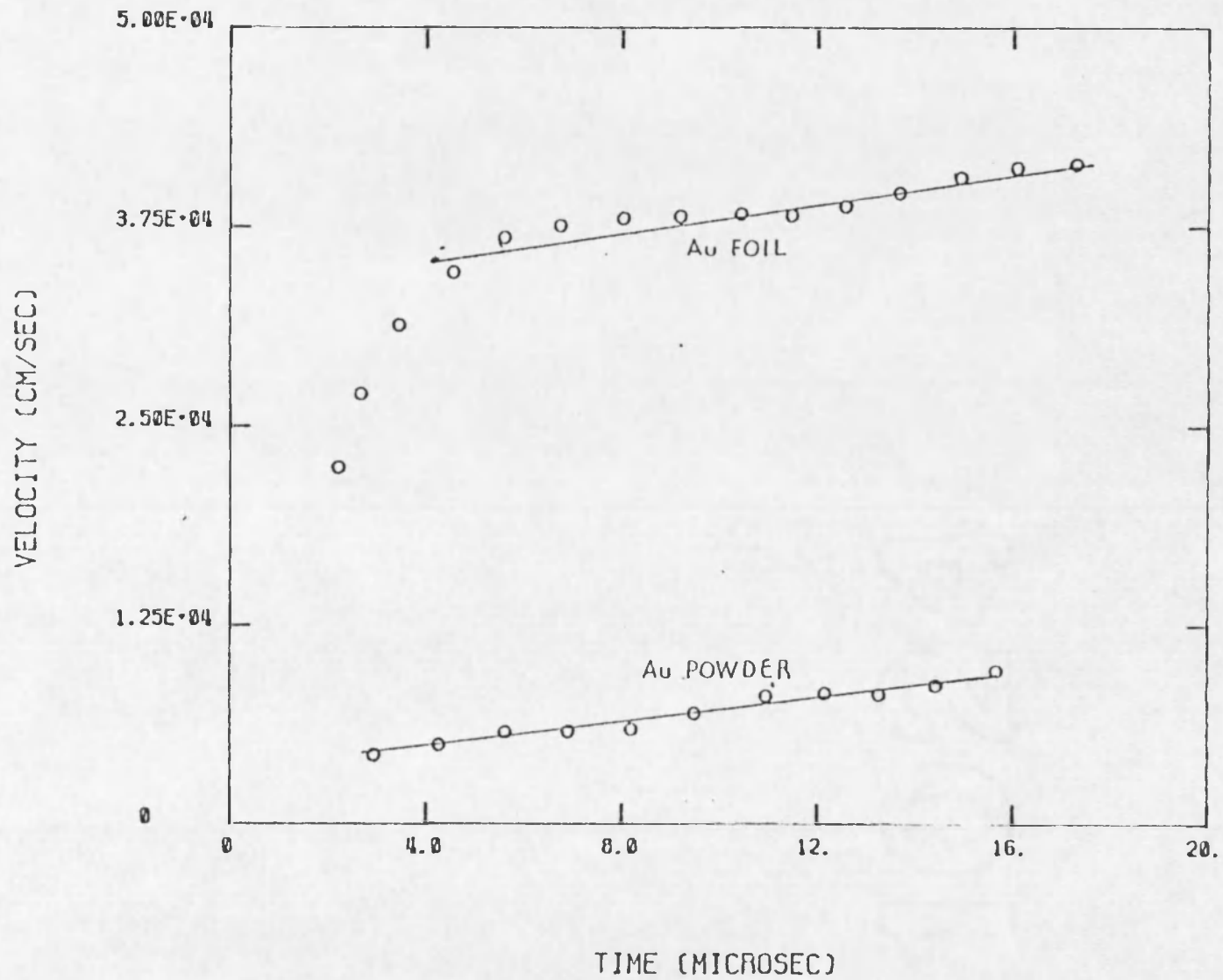


Fig. 15. Velocity as a Function of Time for Two Au Sample Configurations

It is questionable to fit a line to the data and assume deviations are random when such a pattern emerges.

The pattern can be divided into three phases. After an initial rapid acceleration (phase 1), the data levels and begins a slight decrease (phase 2). Then there appears to be another acceleration and leveling (phase 3). This pattern can be seen in Figures 4 and 15. Although FARA does not model the two phase thermal expansion accurately, as seen by the lack of initial acceleration, phase three might be due to a fluid expansion effect. If we assume this to be true, then it is difficult, if not impossible, to separate the effect of the fluid momentum on the piston motion from that of the vapor pressure.

Finally, the FARA code was used to numerically compare Benson's EOS to Menzies' equation of state with the three heat capacity models discussed above. As can be seen from Figures 16-18, the use of Benson's EOS predicts higher vapor pressures for particular specific energy depositions. Model 3, based on statically measured data to 3500K, is much lower than the other two heat capacity models. Menzies' EOS is an accepted relationship when used with the first two heat capacity models.

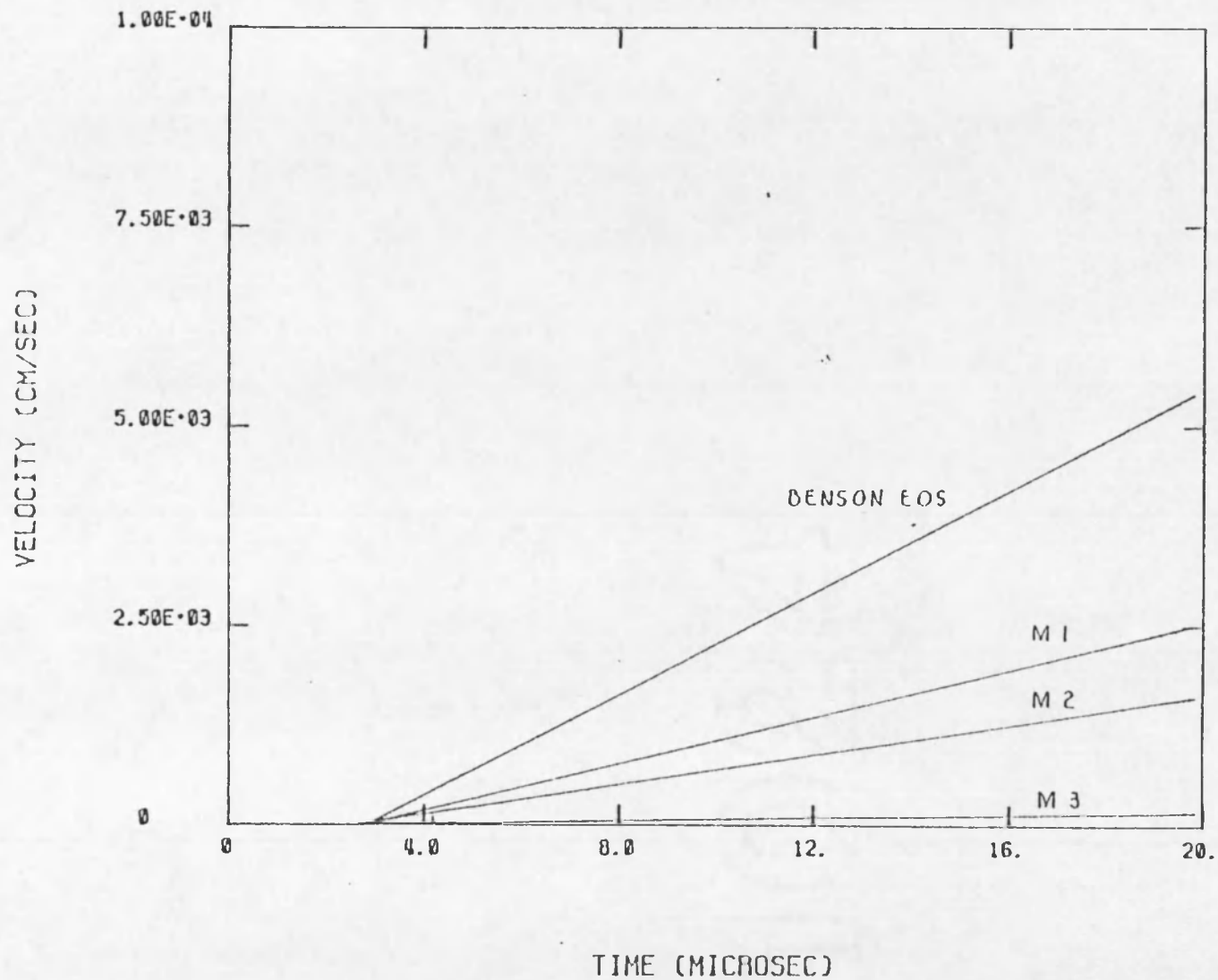


Fig. 16. Comparison of Numerical Results Using Benson's and Menzies' EOS Models for 1860 J/g Energy Pulse.

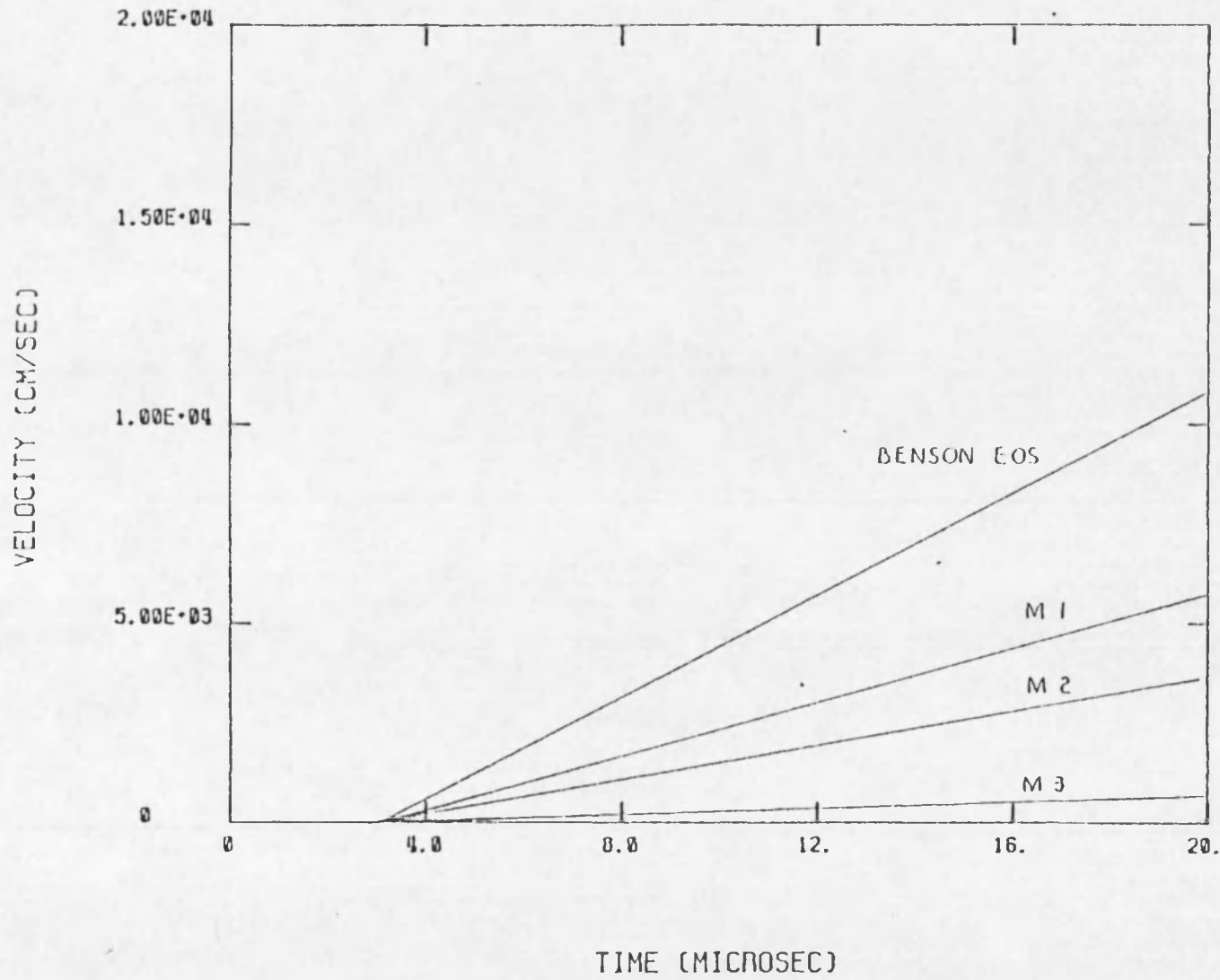


Fig. 17. Comparison of Numerical Results Using Benson's EOS and Menzies EOS with Three Heat Capacity Models for 1990 J/g Energy Pulse.

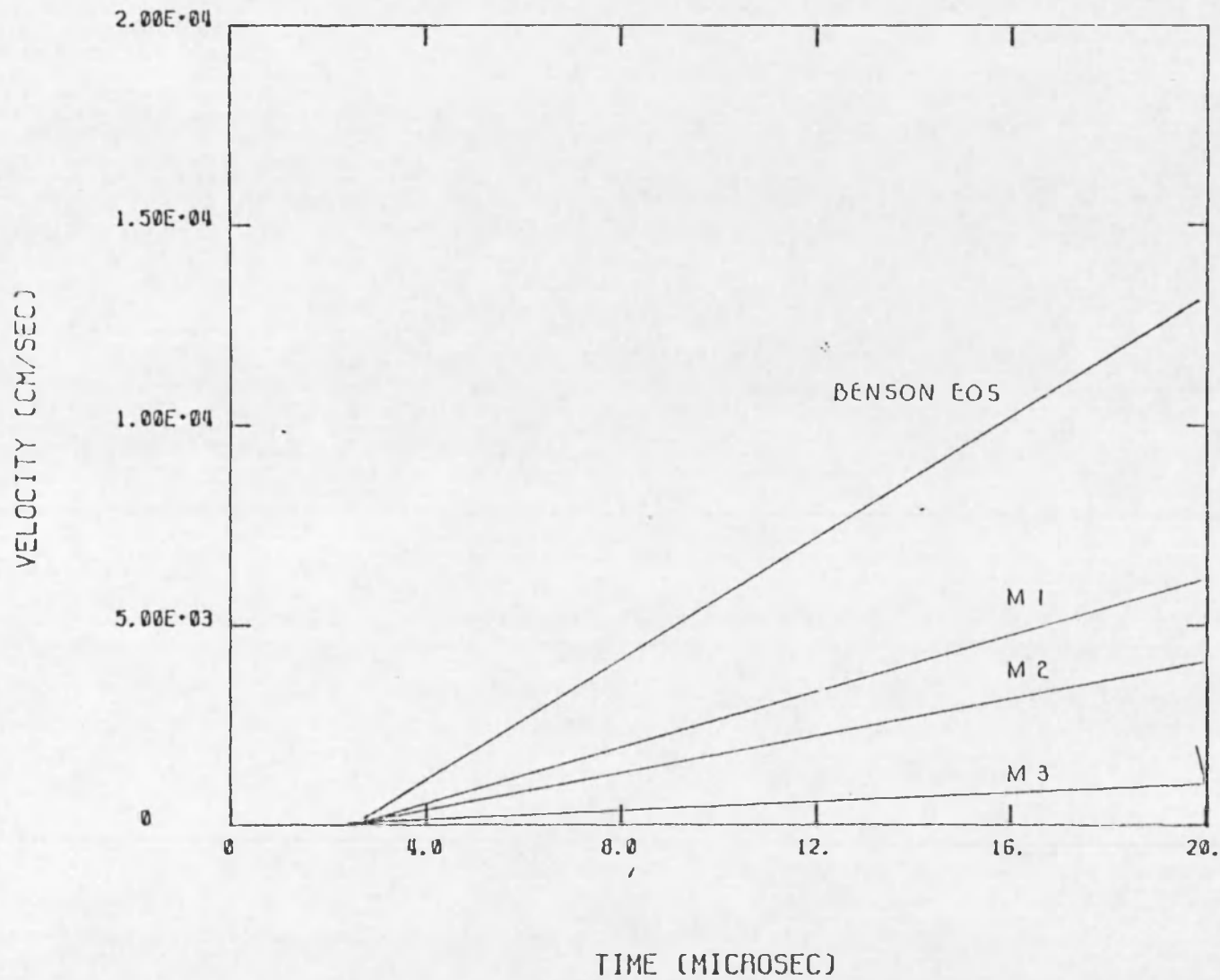


Fig. 18. Comparison of Numerical Results Using Benson's EOS and Menzies EOS with Three Heat Capacity Models for 2030 J/g Energy Pulse.

CHAPTER 5

CONCLUSION

FARA was implemented to model the experimental analysis of the UO_2 experiments performed by Benson. Although it appeared that the numerical results were similar to the experimental, this is attributed to the spatially constant energy deposition term used by the code instead of a profile similar to Figure 3. Because Benson's EOS predicted greater vapor pressures for a specified energy input, there has been some criticism of the results and analysis. Overall, there appears to be two critical areas. The first is his assumption of constant vapor pressure throughout the volume. This allows a one to one relation of specific internal energy to vapor pressure. This assumption is not borne out by the numerical results. Also, Benson assumed the effects of fluid motion and vapor pressure were distinct and separable. Looking at the experimental data, this may not be the case. These assumptions are the foundation of his vapor pressure-specific energy relationship.

If Benson's analysis of the UO_2 data is accurate, then it should be recalled that the comparison of his equation of state to other EOS models is based on a heat capacity model that is accepted by the scientific community, but cannot be considered an accurate representation of heat capacity values over the entire temperature range in question. Final judgment on the accuracy of the relationship

between vapor pressure and specific energy must wait until accurate heat capacity data is obtained for high temperatures. Only then can an accurate comparison be made.

More work needs to be done on the FARA code, before it can be considered as a good hydrodynamics code. Specific improvements might be made in the boundary motion and source input equations. Because FARA is already capable of handling two components, a separated two phase model might provide significant improvements. A major modification would be a conversion to two dimensions. With the above revisions, perhaps FARA could join the realm of the currently used hydrodynamics codes.

APPENDIX A

INPUT DESCRIPTION

The entire data file will be presented in a clear manner in this section. For each data card, the input format and variables will be listed. Also, a description of each variable, its function and value.

Card 1 1216 IZ,N,IT,IPRT,IS

IZ = Number of calculational mesh cells

= 30

N = Number of variables (maximum)

= 12

IT = Number of time steps

IPRT = Print control switch

IS = Number of components (1,2)

= 1

Card 2 1216 ISOU,IDEAL,JXO

ISOU = Energy input switch (on/off)

= 1 (on)

IDEAL = Switch for perfect gas law (on/off)

= 1 (off)

JXO = Number of outer passes

= 3

Card 3 1216 IDEBUG,ITS,ICELL

IDBUG = Print control for debug
 = 0 off
 = 1 every outer pass
 = 2 1+ convergence values
 = 3 2+ equation residues
 = 4 3+ Jacobian matrix and inverse

ITS = Time step for IDEBUG

ICELL = Mesh cell for IDEBUG

Card 4 6E10.0 EX

EX = Maximum error bound
 = 1.0E-05

Card 5 6E10.0 IEXP(I) I=1,12

IEXP = Error bound adjustment factor
IEXP(1) = 1
(3) = 2
(9) = 1

Card 6 6E10.0 DELT

DELT = Time step increment
 = 5.0E-09 sec

Card 7

2012

IVA(I) I=1,12

IVA = Switch for implicit solution variables

IVA(1) = 1 on

(2) = 0 off

(3) = 1

(4) = 0

(5) = 0

(6) = 0

(7) = 0

(8) = 0

(9) = 1

(10) = 0

(11) = 0

(12) = 0

Card 8

2012

IEQ(I) I=1,12

IEQ = Switch for implicit solution equations

IEQ(1) = 1 on

(2) = 0 off

(3) = 1

(4) = 0

(5) = 0

(6) = 0

(7) = 0

(8) = 0

(9) = 1
(10) = 0
(11) = 0
(12) = 0

Card 9 6E10.0 G,AK,AF,AH,SRCO

G = Gravitational coefficient
= 0.0
AK = Drag coefficient
= 0.0
AF = Frictional coefficient
= 0.0
AH = Heat transfer coefficient
= 0.0
SRCO = Peak energy deposition (J/g)
= 1860 to 2030

Cards 10-15 6E10.0 Z(I) I=1,32

Z(I) = Spatial value of right edge of cell I
Z(I) = 0.0
Z(32) = 3.1E-03
DELZ = 1.0E-04 cm

Cards 16-39 6E10.0 X(N,I) I=1,32 N=1,12

X(1,I) = Density of cell I
= 2.0E-03 g/cm³ for all cells

X(3,I) = Velocity of cell I
= 0.0 cm/sec

X(5,I) = Volume fraction of cell I
= 1.0

X(11,I) = Temperature of cell I
= 300.0k

Card 40 6E10.0 AV,BV,CV

AV,BV,CV = Constants for Menzies' EOS
= not used

Cards 41-44 6E10.0 AC(3,3)

AC(I,J) = Array space for various constants
= not used

REFERENCES

- Benson, D. A., Sandia Laboratories Report, SAND-77-0429, Sandia Laboratories, Albuquerque, N. M., (1977).
- Ganapol, B. D., Associate Professor, Dept. Nuclear and Energy Engineering, University of Arizona, Tucson, Ariz., Private Communication, (August 1977).
- Ganapol, B. D., Associate Professor, Dept. Nuclear and Energy Engineering, University of Arizona, Tucson, Ariz., Private Communication, (May 1978).
- Halbleib, J.A., W. H. Vandevender, TIGER, SLA-73-1026, Sandia Laboratories, Albuquerque, N. M., (March 1974).
- Harlow, F. H., A. A. Amsden, Fluid Dynamics, LA-4700, LASL Report, (June 1971).
- Nakamura S., Computational Methods in Engineering and Scheme, Wiley and Sons, (1977).
- Ostenson, R. W., Nuclear Technology, 73, 301, (1979).

